ISPRS Journal of Photogrammetry and Remote Sensing 66 (2011) 484–497

Contents lists available at ScienceDirect

ISPRS Journal of Photogrammetry and Remote Sensing

journal homepage: www.elsevier.com/locate/isprsjprs

Building roof modeling from airborne laser scanning data based on level set approach

KyoHyouk Kim, Jie Shan *

Geomatics Engineering, School of Civil Engineering, Purdue University, West Lafayette, IN 47907, USA

ARTICLE INFO

Article history:
Received 7 June 2010
Received in revised form
10 February 2011
Accepted 17 February 2011
Available online 23 March 2011

Keywords:
LiDAR (Light Detection And Ranging)
Level set
Multiphase level set
Segmentation
Building reconstruction

ABSTRACT

This paper presents a novel approach to building roof modeling, including roof plane segmentation and roof model reconstruction, from airborne laser scanning data. Segmentation is performed by minimizing an energy function formulated as multiphase level set. The energy function is minimized when each segment corresponds to one or several roof plans of the same normal vector. With this formulation, maximum n regions are segmented at a time by applying $\log_2 n$ level set functions. The roof ridges or step edges are then delineated by the union of the zero level contours of the level set functions. In the final step of segmentation, coplanar and parallel roof segments are separated into individual roof segments based on their connectivity and homogeneity. To reconstruct a 3D roof model, roof structure points are determined by intersecting adjacent roof segments or line segments of building boundary and then connected based on their topological relations inferred from the segmentation result. As a global solution to the segmentation problem, the proposed approach determines multiple roof segments at the same time, which leads to topological consistency among the segment boundaries. The paper describes the principle and solution of the multiphase level set approach and demonstrates its performance and properties with two airborne laser scanning data sets.

1. Introduction

The 3D building model is one of the necessary components in various scientific and engineering applications, such as urban planning, virtual reality, telecommunication or emergency response. Over the past two decades, 3D building modeling has been carried out from various kinds of data sources, among which Airborne Laser Scanning (ALS) data gains increasing popularity in recent practices and studies. Due to its capability of measuring both height and planimetric location and its increasingly higher density of up to more than ten (10) points per square meter, detailed roof plane structure as well as building boundary can be precisely determined (Oude Elberink and Vosselman, 2009; Rottensteiner, 2003; Rottensteiner and Briese, 2002; Sampath and Shan, 2010; Verma et al., 2006; Vosselman and Dijkman, 2001; Zhou and Neumann, 2008).

Most reported building modeling approaches follow four common processing steps. First, ground points and non-ground points are separated. This separation can be accomplished through morphological filtering (Arefi and Hahn, 2005; Zhang et al., 2003), labeling process (Shan and Sampath, 2005), and analysis of height texture measures (Oude Elberink and Maas, 2000). More details about various filter algorithms and their experimental comparisons are presented in Sithole and Vosselman (2004). In the second step, identified non-ground points are further processed to remove unwanted points, most of which are returns from trees, cars, or side walls of buildings. These unwanted points can be identified and removed by analyzing the first and last returns (Alharthy and Bethel, 2002), eigenvalue analysis of local covariance matrix (Sampath and Shan, 2010; Verma et al., 2006), or dimensionality learning (Wang and Shan, 2009). The third step is to determine planar roof primitives. Various methods have been studied, including region growing (Rottensteiner, 2003), Hough transform (Maas and Vosselman, 1999; Vosselman and Dijkman, 2001), and RANSAC (RANdom SAmple Consensus) (Tarsha-Kurdi et al., 2008). The main objective of this step is to segment the original point clouds into planar roof primitives based on certain similarity properties. For an overview of different segmentation approaches, we refer the reader to Vosselman et al. (2004). More details on the comparison between RANSAC and Hough transform for roof plane segmentation and their experimental results are presented in Tarsha-Kurdi et al. (2007). The final step is to reconstruct building models, for which there are two

* Corresponding author.
E-mail addresses: kim458@purdue.edu (K. Kim), jshan@purdue.edu, jshan@ecn.purdue.edu (J. Shan).

0924-2716/$ – see front matter © 2011 Published by Elsevier B.V. on behalf of International Society for Photogrammetry and Remote Sensing, Inc. (ISPRS).
doi:10.1016/j.isprsjprs.2011.02.007

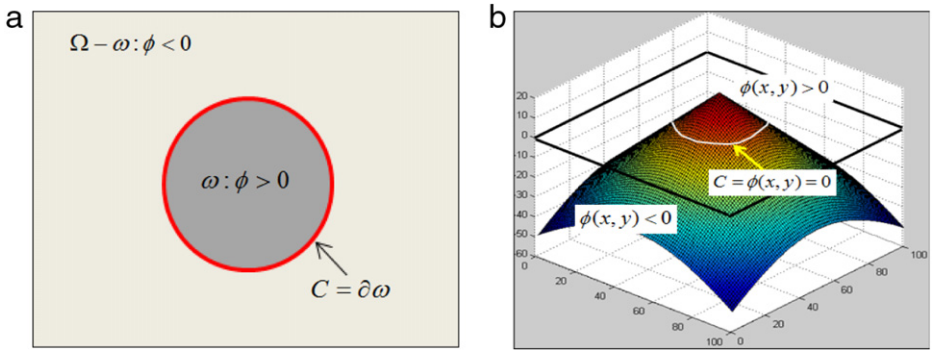

Fig. 1. Implicit representation of the curve C: (a) Curve $C(=\partial\omega)$; (b) Implicit representation of C by the zero level curve of the level set function $\phi(x, y)$.

general approaches: the model-driven and the data-driven. In a model-driven approach, a predefined catalog of roof forms is used to find the best fit for the segmented roof primitives (Maas and Vosselman, 1999). The advantage of this approach is that it can always reconstruct a topologically consistent model. In contrast, if the estimated model is very complex or not included in the predefined roof catalog, its 3D reconstruction process may fail. In data-driven approach, the 3D model is reconstructed by assembling segmented individual roof planes. One of the difficult issues in this method is to determine the topologic relations among the detected roof segments. To this end, roof topology is described by a graph or adjacency matrix (Forlani et al., 2006; Oude Elberink and Vosselman, 2009; Sampath and Shan, 2010; Verma et al., 2006), based on which roof structures, e.g., intersections of adjacent roof segments, including roof ridges and corner points, can be determined.

While most existing approaches show promising results towards 3D building modeling, there are still a number of issues to be improved. In the context of segmentation (either from digital surface model or LiDAR points), segmented roofs are mostly disconnected, which leads to confusion for determining the neighborhood relations among roof segments. Furthermore, locating height discontinuities (step edges) only from LiDAR points is also difficult and requires additional information or constraint. To resolve these issues, we introduce a novel approach to roof segmentation and reconstruction. It formulates the region-based segmentation under the framework of level set method. Level set method itself has been widely used in computer vision community for image segmentation. However, only a few were for remote sensing applications, such as boundary extraction between different natural features. (Zhang and Jiang, 2008), segmentation of SAR imagery (Ayed et al., 2005; Horritt, 1999), detection of man-made objects (Cao et al., 2005) and building boundary extraction (Cao and Yang, 2007; Karantzalos and Paragios, 2008; Song and Shan, 2008) from either satellite or aerial images. At the time of writing, we are not aware of reported applications of level set method for airborne laser ranging data segmentation. It has not been fully studied and evaluated in topographic remote sensing for either imagery or ranging data.

Comparing with other building modeling methods, the proposed approach, though implemented in a gridded spatial domain, does not resample the original point clouds such that the accuracy of original data is retained. Multiphase level set formulation allows for segmentation of multi-regions in one run. Furthermore, the segmentation process can also be implemented recursively and does not need a priori knowledge on building structure. Finally, segmented roof planes are always connected without gap or empty region, which represents the same topologic relations as that of the given roof form. This defines the roof structures and supports roof reconstruction. Like most other studies, this paper also assumes polyhedral buildings and thus focuses on segmenting planar roof elements. Since airborne LiDAR points lie mostly on the building roof tops and only a small fraction of points is from side walls of buildings, the final 3D building model is represented by extruding the reconstructed roof shape. As a result, some buildings with complex 3D structures like overhangs may not be accurately reconstructed.

The proposed approach is summarized below. It starts with determining normal vectors of each LiDAR point of the building. Local planarity at each point is analyzed to exclude non-planar points lying on roof ridges or step edges. Initial level set functions represented as surfaces are defined in the underneath 2D Cartesian grid enclosing all building points. The segmentation process, formulated as an energy minimization problem with multiphase level set divides this 2D grid into multiple homogeneous regions with similar normal vectors. As the result of this segmentation, topological relations among different roof segments are determined by using the segmented Cartesian grid (i.e., a labeled image). Finally, roof segments and their topologic relations are used to reconstruct the 3D roof model.

The remainder of this paper is as follows. Section 2 describes the principles of level set method and its recent extension to multiphase and multichannel setup. Section 3 discusses roof plane segmentation based on this method, while Section 4 determines the roof topology and reconstruction. Results from two different data sets are presented and evaluated in Section 5. Section 6 presents the final conclusion on this approach.

2. Principles

2.1. Level set method

Osher and Sethian (1988) introduced level set method to describe evolving curves and surfaces. It has then been widely used in a variety of image segmentation and boundary detection problems in computer vision. The main idea is to embed the evolving curves or surfaces in a space of one dimension higher. As the most important advantage, level set method allows for topological changes of the evolving curves, such as merging and breaking. Let Ω be a fixed rectangular grid in R^2. A two dimensional image u_0 is then defined as $u_0 : \Omega \rightarrow R$. We consider the evolving curve C in Ω as the boundary of an open subset $\omega \in \Omega$, i.e., $C = \partial\omega$ as shown in Fig. 1(a). In level set approach, the boundary C is represented implicitly as the zero level curve of one higher Lipschitz function ϕ as shown in Fig. 1(b), such that

$$\begin{aligned} &\phi(x, y) > 0 \quad \text{in } \omega \\ &\phi(x, y) < 0 \quad \text{in } \Omega - \omega \\ &\phi(x, y) = 0 \quad \text{on } \partial\omega = C. \end{aligned} \tag{1}$$

The function ϕ is called level set function and represented as a signed distance function for practical purpose as shown in Fig. 1(b). The deformation of the evolving curve C is represented

by introducing a time viable t to the level set function such that

$$\frac{\partial \phi(x,y,t)}{\partial t} = F|\nabla\phi| \quad \text{with } \phi(x,y,0) = \phi_0(x,y) \tag{2}$$

where t denotes evolving time, $\phi_0(x,y) = 0$ defines the initial level set functions at $t = 0$, F is the speed for curve propagation, and ∇ is the gradient operator. This equation describes the propagation of the curve C with speed F. A special case is the motion by mean curvature K, which is used to describe many physical phenomena, such as burning flames and crystal growth (Sethian, 1990).

For image segmentation, the evolving curve C needs to be stopped at the object boundary to be detected. This can be handled in two different ways by (1) applying an edge-stopping function, or (2) minimizing an energy function. The edge-stopping function stops the curve evolving at the object boundary. However, this is reliable only when the object boundary has a strong gradient. When noise or insignificant gradient exists, the evolving curve may not stop at the object boundary. Another drawback of this approach is that it allows for only one-way curve evolution, namely shrinking or growing based on the sign of F. Therefore, a priori knowledge about object boundary is required to determine an initial zero level curve and its propagation direction.

To resolve these issues, the region-based (also called energy based) level set method was proposed by Chan and Vese (2001). In this approach, the propagation of a curve is halted based on the energy minimization criterion. For a given image u_0 with only two regions as shown in Fig. 1(a), the energy function E is defined as follows

$$E = \mu \cdot \text{Length}(C) + \nu \cdot \text{Area}(C_{\text{in}}) + F(C_{\text{in}}) + F(C_{\text{out}}) \tag{3}$$

where C is the boundary of an open subset $\omega \in \Omega$, $\mu \geq 0$, $\nu \geq 0$ are fixed weight factors, and $C_{\text{in}}, C_{\text{out}}$ represent the inside and outside region of the curve, respectively. The two fitting terms $F(C_{\text{in}})$ and $F(C_{\text{out}})$ are defined in Eq. (4) such that they have minimum values when the curve C lies on the object boundary.

$$\begin{aligned} F(C_{\text{in}}) &= \lambda_1 \int_{C_{\text{in}}} (u_0 - c_1)^2 \mathrm{d}x\mathrm{d}y \\ F(C_{\text{out}}) &= \lambda_2 \int_{C_{\text{out}}} (u_0 - c_2)^2 \mathrm{d}x\mathrm{d}y \end{aligned} \tag{4}$$

where $\lambda_1 > , \lambda_2 > 0$ are fixed weight factors and c_1, c_2 are respectively the average intensity (or other feature) values inside and outside the curve C. It is seen that the above energy function E of Eq. (3) is minimized when the curve C lies on the object boundary because the two fitting terms vanish.

To incorporate the level set principle into this minimization problem, the Heaviside function $H(z)$ and delta function $\delta(z)$ are introduced.

$$\begin{aligned} H(x) &= \begin{cases} 1 & \text{if } x \geq 0 \\ 0 & \text{if } x < 0 \end{cases} \\ \delta(x) &= H'(x) = \frac{\mathrm{d}}{\mathrm{d}x} H(x). \end{aligned} \tag{5}$$

Assuming the level set function ϕ takes $(+)$ and $(-)$ values inside and outside the curve C respectively, its Length(C) and Area(C_{in}) can be represented as

$$\begin{aligned} \text{Area}(C_{\text{in}}) &= \int_{\Omega} H(\phi(x,y))\mathrm{d}x\mathrm{d}y \\ \text{Length}(C) &= \int_{\Omega} |\nabla H(\phi(x,y))|\mathrm{d}x\mathrm{d}y \\ &= \int_{\Omega} \delta(\phi(x,y))|\nabla\phi(x,y)|\mathrm{d}x\mathrm{d}y. \end{aligned} \tag{6}$$

The area expression above essentially counts the number of '1's inside the curve, while the length expression counts the number of '1's along the boundary. In a similar way, the two fitting terms $F(C_{\text{in}})$ and $F(C_{\text{out}})$ can be rewritten as

$$\begin{aligned} F(C_{\text{in}}) &= \lambda_1 \int_{\Omega} (u_0 - c_1)^2 H(\phi(x,y))\mathrm{d}x\mathrm{d}y \\ F(C_{\text{out}}) &= \lambda_2 \int_{\Omega} (u_0 - c_2)^2 (1 - H(\phi(x,y)))\mathrm{d}x\mathrm{d}y. \end{aligned} \tag{7}$$

Inserting Eqs. (6) and (7) into the energy function of Eq. (3), we have

$$\begin{aligned} E = {} & \mu \int_{\Omega} \delta(\phi(x,y))|\nabla H(\phi(x,y))|\mathrm{d}x\mathrm{d}y + \nu \int_{\Omega} H(\phi(x,y))\mathrm{d}x\mathrm{d}y \\ & + \lambda_1 \int_{\Omega} (u_0 - c_1)^2 H(\phi(x,y))\mathrm{d}x\mathrm{d}y \\ & + \lambda_2 \int_{\Omega} (u_0 - c_2)^2 (1 - H(\phi(x,y)))\mathrm{d}x\mathrm{d}y. \end{aligned} \tag{8}$$

Note that the integral range in Eq. (8) is extended to the whole image domain Ω by introducing the Heaviside function. To minimize Eq. (8), we first derive an Euler–Lagrange equation. Keeping c_1 and c_2 fixed and minimizing the energy function E with respect to ϕ, the corresponding Euler–Lagrange equation for ϕ can then be derived. Parameterizing the descent direction by an artificial time $t \geq 0$, the Euler–Lagrange equation can be written as

$$\begin{aligned} \frac{\partial \phi}{\partial t} = \delta(\phi) \Bigg[& \mu \cdot \text{div}\left(\frac{\nabla\phi}{|\nabla\phi|}\right) - \nu \\ & - \lambda_1 (u_0 - c_1)^2 + \lambda_2 (u_0 - c_2)^2 \Bigg]. \end{aligned} \tag{9}$$

The level set function ϕ will be determined by solving the above partial differential equation, for which a finite difference technique in the discrete domain will be presented in Section 2.3.

2.2. Multiphase and multichannel level set

This section considers a more general case in which there exist more than two regions to be segmented or more than one data layer (or channel) is involved in the segmentation process. To segment more than two regions, the aforementioned approach (called two-phase level set, i.e., one phase represents the inside and the other outside of the zero level curve) needs to be extended. Several authors have proposed different formulations to handle a larger number of phases. Zhao et al. (1996) use one separate level set function for each region. To keep the phases disjoint and their union being the entire domain Ω, additional constraint term is added to the energy function. The development of Vese and Chan (2002) considers overlap and vacuum as separate regions. As shown in Fig. 2(a), the two level set functions with overlap divide Ω into four separate regions. In the same manner, eight separate regions can be represented by three level set functions as shown in Fig. 2(b) Therefore, $\log_2 n$ level set functions are required to represent n regions. In Fig. 2, R10 represents the region satisfying the following condition: $\phi_1(x,y) > 0$ and $\phi_2(x,y) < 0$. Similar rules also apply to regions defined by three level set functions.

The energy function for multiphase level set can be formulated in a similar way as in Eq. (8), e.g., the energy function for two level set functions is

$$\begin{aligned} E = {} & \lambda_1 \int_{\Omega} (u_0 - c_{11})^2 H(\phi_1) H(\phi_2)\mathrm{d}x\mathrm{d}y \\ & + \lambda_2 \int_{\Omega} (u_0 - c_{10})^2 H(\phi_1)(1 - H(\phi_2))\mathrm{d}x\mathrm{d}y \end{aligned}$$

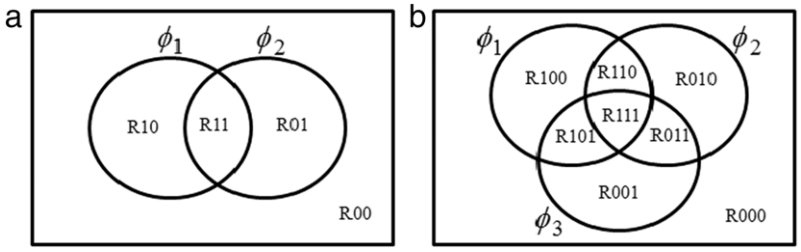

Fig. 2. Regions represented by multiphase level set functions: (a) Four regions by two level set functions; (b) Eight regions by three level set functions.

$$
\begin{aligned}
&+\lambda_3\int_\Omega (u_0-c_{01})^2(1-H(\phi_1))H(\phi_2)\mathrm{d}x\mathrm{d}y\\
&+\lambda_4\int_\Omega (u_0-c_{00})^2(1-H(\phi_1))(1-H(\phi_2))\mathrm{d}x\mathrm{d}y\\
&+\nu_1\cdot\int_\Omega H(\phi_1)\mathrm{d}x\mathrm{d}y+\nu_2\cdot\int_\Omega H(\phi_2)\mathrm{d}x\mathrm{d}y\\
&+\mu_1\cdot\int_\Omega |\nabla H(\phi_1)|\mathrm{d}x\mathrm{d}y+\mu_2\cdot\int_\Omega |\nabla H(\phi_2)|\mathrm{d}x\mathrm{d}y
\end{aligned}
\tag{10}
$$

where $c_{11}, c_{10}, c_{01}, c_{00}$ represent the average feature values (such as intensity) of the four regions and $\lambda_{i=1,2}$, $\nu_{i=1,2}$ and $\mu_{i=1,2}$ are fixed weight factors. When multiple channels, such as RGB color images, are involved for segmentation, the energy function is represented as

$$
\begin{aligned}
E=\ &\lambda_1\int_\Omega \|\boldsymbol{u}_0-\boldsymbol{c}_{11}\|^2H(\phi_1)H(\phi_2)\mathrm{d}x\mathrm{d}y\\
&+\lambda_2\int_\Omega \|\boldsymbol{u}_0-\boldsymbol{c}_{10}\|^2H(\phi_1)(1-H(\phi_2))\mathrm{d}x\mathrm{d}y\\
&+\lambda_3\int_\Omega \|\boldsymbol{u}_0-\boldsymbol{c}_{01}\|^2(1-H(\phi_1))H(\phi_2)\mathrm{d}x\mathrm{d}y\\
&+\lambda_4\int_\Omega \|\boldsymbol{u}_0-\boldsymbol{c}_{00}\|^2(1-H(\phi_1))(1-H(\phi_2))\mathrm{d}x\mathrm{d}y\\
&+\nu_1\cdot\int_\Omega H(\phi_1)\mathrm{d}x\mathrm{d}y+\nu_2\cdot\int_\Omega H(\phi_2)\mathrm{d}x\mathrm{d}y\\
&+\mu_1\cdot\int_\Omega |\nabla H(\phi_1)|\mathrm{d}x\mathrm{d}y+\ \mu_2\cdot\int_\Omega |\nabla H(\phi_2)|\mathrm{d}x
\end{aligned}
\tag{11}
$$

where $\boldsymbol{u}_0$ is the input multiple channel image, and $\boldsymbol{c}_{11}, \boldsymbol{c}_{10}, \boldsymbol{c}_{01}, \boldsymbol{c}_{00}$ are the average feature values of the four regions. In the same manner as deriving Eq. (9), the corresponding partial derivative equation for each level function can be derived. For example, $\phi_1(x, y, t)$ is given by

$$
\begin{aligned}
\frac{\partial\phi_1}{\partial t}=\ &\delta(\phi_1)\left\{\mu_1\cdot\mathrm{div}\left(\frac{\nabla\phi_1}{|\nabla\phi_1|}\right)-\nu_1\right.\\
&+(\lambda_3\|\boldsymbol{u}_0-\boldsymbol{c}_{01}\|^2-\lambda_1\|\boldsymbol{u}_0-\boldsymbol{c}_{11}\|^2)H(\phi_2)\\
&\left.-(\lambda_2\|\boldsymbol{u}_0-\boldsymbol{c}_{10}\|^2-\lambda_4\|\boldsymbol{u}_0-\boldsymbol{c}_{00}\|^2)(1-H(\phi_2))\right\}.
\end{aligned}
\tag{12}
$$

2.3. Numerical solution

To solve the partial derivative equations of Eq. (9) or (12) in the discrete domain, the finite difference technique is used. We assume that the input image u_0 is an $M\times N$ grid with one channel. Let h be the space step, Δt the time step, $(x_i, y_j) = (ih, jh)$ the grid point, for $1\le i\le N$ and $1\le j\le M$ and $\phi(i,j)=\phi(x_i,y_j)$. Then, $\nabla\phi$ can be estimated by central difference, i.e.

$$
\begin{aligned}
\nabla\phi&=\left(\frac{\partial\phi}{\partial x},\frac{\partial\phi}{\partial y}\right),\\
\phi_x&=\frac{\partial\phi}{\partial x}\approx\frac{\phi(i+1,j)-\phi(i-1,j)}{2\Delta x},\\
\phi_y&=\frac{\partial\phi}{\partial y}\approx\frac{\phi(i,j+1)-\phi(i,j-1)}{2\Delta y}.
\end{aligned}
\tag{13}
$$

As for the divergence term in Eqs. (9) and (12), the mean curvature K is used

$$
K=\mathrm{div}\left(\frac{\nabla\phi}{|\nabla\phi|}\right)=\frac{\phi_{xx}\phi_y^2-2\phi_x\phi_y\phi_{xy}+\phi_{yy}\phi_x^2}{(\phi_x^2+\phi_y^2)^{3/2}}
\tag{14}
$$

where ϕ_{xx}, ϕ_{yy} and ϕ_{xy} denote the second partial derivatives of ϕ. To find global minimum with fast convergence, the Heaviside function $H(\phi)$ is regularized (Chan and Vese, 2001; Vese and Chan, 2002)

$$
H_\varepsilon(x)=\frac{1}{2}\left(1+\frac{2}{\pi}\arctan\left(\frac{x}{\varepsilon}\right)\right),\qquad \delta_\varepsilon=\frac{\mathrm{d}}{\mathrm{d}x}H_\varepsilon(x)
\tag{15}
$$

where ε is a tunable parameter determining the numerical smearing. Approximating the time derivative with the forward difference scheme, Eq. (12) is finally written as follows

$$
\begin{aligned}
\phi_1^{n+1}=\ &\phi_1^n+\Delta t\cdot\delta_\epsilon(\phi_1^n)\{\mu_1\cdot K_1-\nu_i\\
&+(\lambda_3\|\boldsymbol{u}_0-\boldsymbol{c}_{01}\|^2-\lambda_1\|\boldsymbol{u}_0-\boldsymbol{c}_{11}\|^2)H_\varepsilon(\phi_2^n)\\
&-(\lambda_2\|\boldsymbol{u}_0-\boldsymbol{c}_{10}\|^2-\lambda_4\|\boldsymbol{u}_0-\boldsymbol{c}_{00}\|^2)(1-H_\varepsilon(\phi_2^n))\}
\end{aligned}
\tag{16}
$$

where ϕ_1^n is an approximation of ϕ_1 at time $n(\Delta t)$. Using this evolving equation, new approximation of ϕ_1^{n+1} is determined iteratively from ϕ_1^n. In Eq. (16), $\phi_1, H_\varepsilon(\phi_1), \delta_\varepsilon(\phi_1), K_1$ and u_0 have the same dimension and can be considered as an $M\times N$ matrix. Therefore, once we determine $\boldsymbol{c}_{11}, \boldsymbol{c}_{10}, \boldsymbol{c}_{01}, \boldsymbol{c}_{00}, K_1, H_\varepsilon(\phi_1^n)$ and $\delta_\varepsilon(\phi_1^n)$, new approximation ϕ_1^{n+1} is updated with Eq. (16). The same applies for ϕ_2. For detailed discretization and iterative algorithm, we refer the reader to Rudin et al. (1992), Aubert and Vese (1997) and Vese and Chan (2002).

3. Roof segmentation

This section describes the segmentation process based on the level set principles. The local planarity of each LiDAR point is analyzed and normal vectors of planar points are used for segmentation. The segmentation is carried out in a 2D grid enclosing all building points by applying two level set functions such that the 2D grid is divided into four disjoint regions. Each of the four regions corresponds to one or several planar roof segments. This process can be applied recursively for more complex building roofs. Finally, the separation of coplanar and parallel roof segments is discussed.

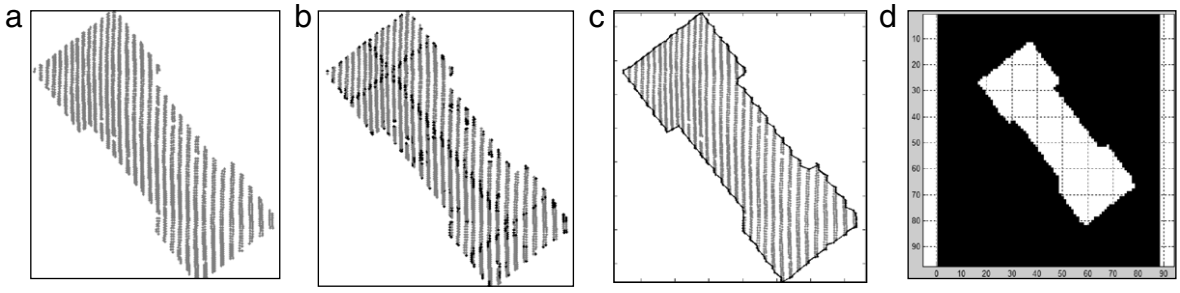

Fig. 3. Pre-processing step: (a) All building points; (b) Planar points (gray) and non-planar points (black); (c) 2D grid Ω with boundary points (black dots); (d) Mask grid Ω_m.

3.1. Normal vector calculation

Any plane π in R^3 is represented uniquely by its normal vector and distance to the coordinate origin. Therefore, most approaches use normal vectors as the homogeneity criterion for planar roof segmentation. For a data point $\boldsymbol{p}_i$, its normal vector is taken as the average of those of its incident triangles. To prevent inaccurate normal calculations, this study further considers the distance between the given point and neighboring points. If one or more sides of an incident triangle T_j are larger than two times the LiDAR ground spacing, its normal vector N_{T_j} is not included for calculation. To identify non-planar points, such as those at roof ridges or building boundary, PCA (Principal Component Analysis) or dimensionality analysis were used (Sampath and Shan, 2010; Verma et al., 2006). Another approach used in this study is to analyze the angular differences of the normal vectors. To check if a point $\boldsymbol{p}_i$ is a planar point, we calculate MAD (Mean Angle Difference) of N_{p_i} with N_{T_j} of neighboring triangles as follows

$$\text{Mean Angle Difference} = \frac{1}{n}\sum_{j=1}^{n} N_{p_i} \cdot N_{T_j} \tag{17}$$

where n is the number of triangles incident to p_i and $(\cdot)$ denotes an inner product of two vectors. Ideally, MAD should be zero if $\boldsymbol{p}_i$ lies on the perfect plane spanned by neighboring triangles. However, due to the inherent data noise and non-planarity of the object, certain angle threshold (20° in this study) is applied. The identified planar points and their normal vectors are then used for the subsequent segmentation process.

3.2. Plane direction segmentation

Let $\boldsymbol{P}$ be planar points and N be their normal vectors. We use N as input feature vectors to level set approach, with n_x, n_y and n_z forming three channels. Two level set functions are involved for segmentation, i.e., up to four regions can be segmented at one time. First, we specify a 2D grid Ω enclosing $\boldsymbol{P}$ with cell size Δg. The cell size is determined from the average point density d_p satisfying $\Delta g = 1/\sqrt{d_p}$. Therefore, the number of cells is approximately equal to that of LiDAR points of the building. Different cell sizes may possibly lead to different segmentation results. Generally, a large cell size produces a coarse segmentation and some small features may not be retained. In contrast, a small cell size leads to a fine segmentation at a cost of data redundancy, more storage and computation time. It is considered that a cell size similar to the original LiDAR ground spacing produces the most accurate results (Behan, 2000). Two initial level set functions ϕ_1 and ϕ_2 (see Section 5.3) are defined from a set of regularly spaced zero level curves in Ω. Building boundary points are then determined using the α-shape algorithm (Edelsbrunner et al., 1983; Sampath and Shan, 2007; Wei, 2008), which forms a mask grid Ω_m to avoid calculation outside the building boundary. Fig. 3 is used to illustrate this process.

In the subsequent step, segmentation is carried out iteratively to divide Ω_m into four disjoint regions Ω_i $(1 \le i \le 4)$, each of which represents a spatial extent with the similar normal vectors. It should be noted that a region may consist of either one roof segment or a group of roof segments with the same normal vectors. The roof segments of one region Ω_i need not to be spatially connected. The energy function to be minimized is Eq. (11), where $\boldsymbol{u}_0$ is determined from the calculated normal vectors N by linear interpolation, $\boldsymbol{c}_{11}, \boldsymbol{c}_{10}$ etc. are the mean normal vectors in the corresponding regions. As an example, for region R10 we have

$$\boldsymbol{c}_{10} = \frac{1}{k}\sum_{i=1}^{k} N_i, \quad \text{for } \forall i : \phi_1(\boldsymbol{p}_i(x,y)) \ge 0 \text{ and } \phi_2(\boldsymbol{p}_i(x,y)) < 0 \tag{18}$$

where k is the number of points of region R10, $\phi_1(\boldsymbol{p}_i(x,y))$ and $\phi_2(\boldsymbol{p}_i(x,y))$ are evaluations of ϕ_1 and ϕ_2 respectively at a data point $\boldsymbol{p}_i(x,y)$. The numerical solution to the final evolving equation is based on Eq. (16). In this study, we use $\Delta t = 0.01, \varepsilon = 1.5, \mu_{i=1,2} = 0.01 \times 255^2, \nu_{i=1,2} = 0$ and $\lambda_{i=1-4} = 1$ with $\phi_1^0(x,y), \phi_2^0(x,y)$ as initial level set functions. Among these parameters, Δt and μ affect the quality and performance of segmentation. A large Δt can speed up the evolution, but may lead to incorrect segmentation results. Similarly, μ defines the scale of this method; a small value can detect small objects and vice versa. In summary, the segmentation process can be outlined as follows.

- Specify Ω with cell size Δg. The number of rows and columns depends on the average point density.
- Extract building boundary points and create a mask grid Ω_m.
- Initialize two level set functions ϕ_1^0 and ϕ_2^0 using the signed distance functions.
- Repeat the following steps until convergence or for a given number of iterations.
  - Compute $H_\varepsilon(\phi_i^n)$ and $\delta_\varepsilon(\phi_i^n)$ using Eq. (15).
  - Compute the mean curvatures K_i using Eq. (14).
  - Compute the mean normal vectors of four regions, i.e., $\boldsymbol{c}_{11}, \boldsymbol{c}_{10}, \boldsymbol{c}_{01}$ and $\boldsymbol{c}_{00}$ for each ϕ_i^n.
  - Update new ϕ_1^{n+1} and ϕ_2^{n+1} using Eq. (16).
  - Check convergence.

The intermediate plots and final segmentation results are presented in Fig. 4. Fig. 4(a)–(d) show the variations of two zero level curves and four regions from their initial setup (Fig. 4(a)). Four segmented regions $\Omega_i (1 \le i \le 4)$ are presented as a labeled image in Fig. 4(d) with different colors. Each region can also be represented (or extracted) separately using the definition of multiphase level set. For example, Ω_1 (=R11) and Ω_2 (=R10) are determined with grid cells satisfying $\{\Omega_1(x,y) : \phi_1(x,y) \ge 0$ and $\phi_2(x,y) \ge 0\}$ and $\{\Omega_2(x,y) : \phi_1(x,y) \ge 0$ and $\phi_2(x,y) < 0\}$, respectively. It should be noted that the outcome of the above step also generates the roof ridges, which are represented as the union of two zero level curves as shown in Fig. 4(d).

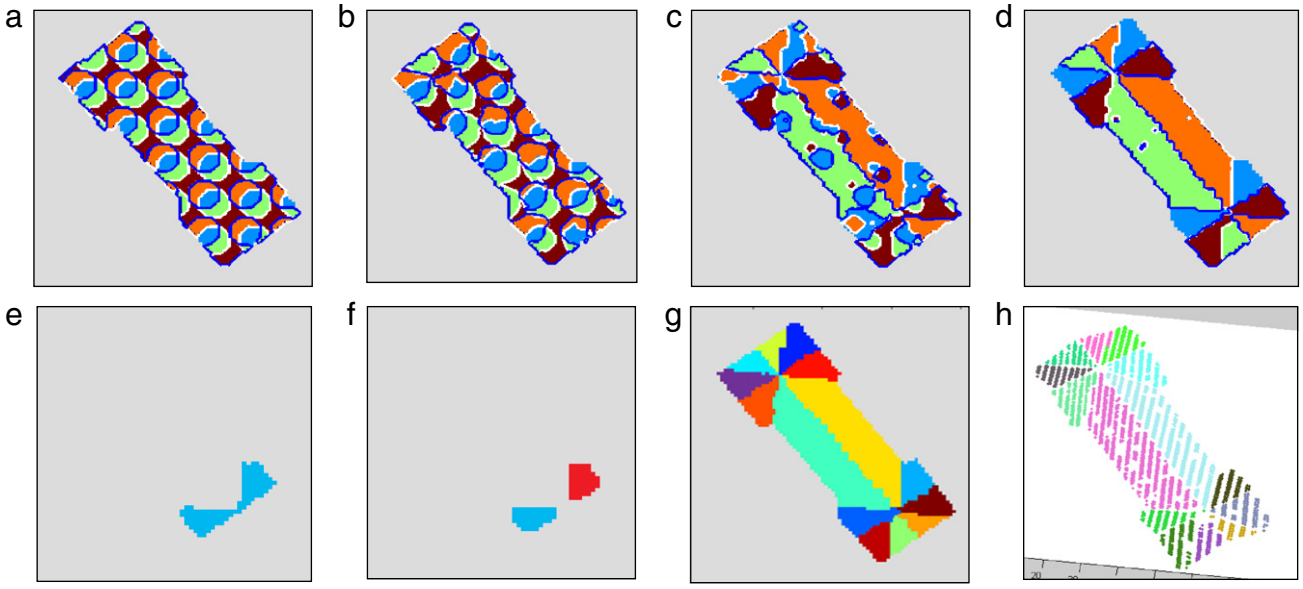

Fig. 4. Segmentation results: (a)–(d) Intermediate plots of four regions (Ω_i) and two zero level curves (black and whites lines) at different iteration steps (1,4,7 and 10); (e) and (f) Separation of misconnected segments; (g) Separated roof planes; (h) Segmented points.

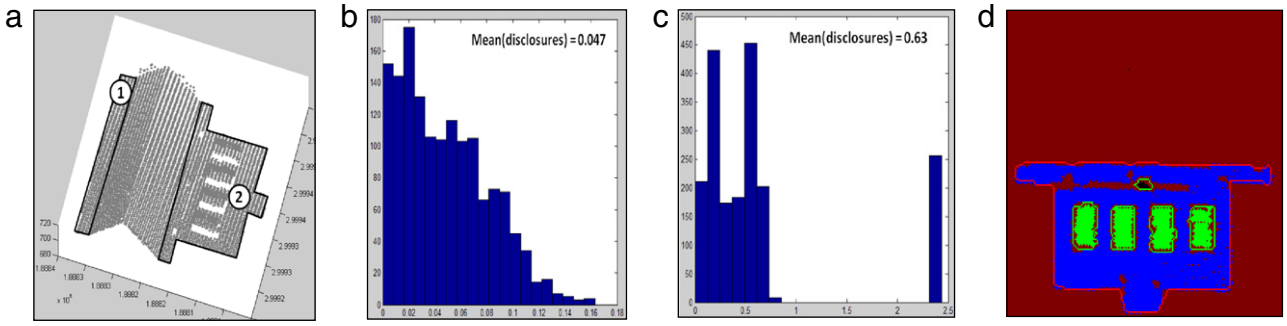

Fig. 5. Separation of parallel planes: (a) Two separated coplanar planes; (b) and (c) Histograms of disclosures of plane "1" and "2"; (d) Separated parallel planes.

3.3. Roof segment separation

In the segmentation outcome shown in Fig. 4(d), roof segments with the same direction are grouped. This section further separates these planes, e.g., coplanar or parallel planes, into individual roof segments.

Coplanar planes have the same mathematical formulation but are spatially separated. Every segmented region Ω_i in Fig. 4(d) consists of a few coplanar planes. Their separation can be performed by density clustering and connectivity analysis in the original data space (Sampath and Shan, 2010). In a 2D grid, a simple connectivity analysis with four or eight neighbors (Haralick and Shapiro, 1992) can be applied. In this study, connectivity analysis with four neighbors is applied to each segment Ω_i. In case a few coplanar segments meet at one pixel (Fig. 4(e)), they are separated by applying morphological opening as shown in Fig. 4(f). For small segments, they are merged with adjacent larger ones. From this process, Ω_i and corresponding point sets $\boldsymbol{P}_i$ are further separated into a total of 14 roof segments as shown in Fig. 4(g) and (h), which are denoted as $\bar{\Omega}_i$ and $\bar{\boldsymbol{P}}_i$ hereafter.

Once coplanar planes are separated, we check the existence of parallel planes in each segment $\bar{\Omega}_i$. First, the mean disclosure of $\bar{\Omega}_i$ is determined by plugging data points $\boldsymbol{p} \in \bar{\boldsymbol{P}}_i$ into the corresponding plane equation. If the mean disclosure of $\bar{\Omega}_i$ is beyond a certain threshold, $\bar{\Omega}_i$ is considered to have parallel planes. Then, segmentation is applied to $\bar{\Omega}_i$ with corresponding disclosures as the feature vectors. Fig. 5 is used to show this process. Roof segment marked as "1" in Fig. 5(a) consists of only one plane, whereas roof segment "2" consists of two groups of parallel planes, i.e., the upper four coplanar planes and the lower, enclosing one. Their mean disclosures are respectively 0.047 m and 0.63 m as shown in Fig. 5(b) and (c) Because of its significant disclosure, the segment "2" is further separated until each newly separated roof segment satisfies a predefined disclosure threshold. The separated two groups of parallel planes are shown in Fig. 5(d) with dark and light gray. Finally, the upper four small coplanar planes are separated into individual roof segments through connectivity analysis.

4. Roof reconstruction

This section describes the reconstruction of a 3D roof model from the above segmentation result by determining the vertices of each roof segment and their connectivity. We call those vertices roof structure points hereafter. These points are mostly induced by the intersection of at least three non-parallel planes and can be determined from the segmentation outcome of the above step.

4.1. Identification of roof structure points

First, we analyze the adjacency among the roof segments to identify roof structure points. We subdivide $\bar{\Omega}$ with grid interval

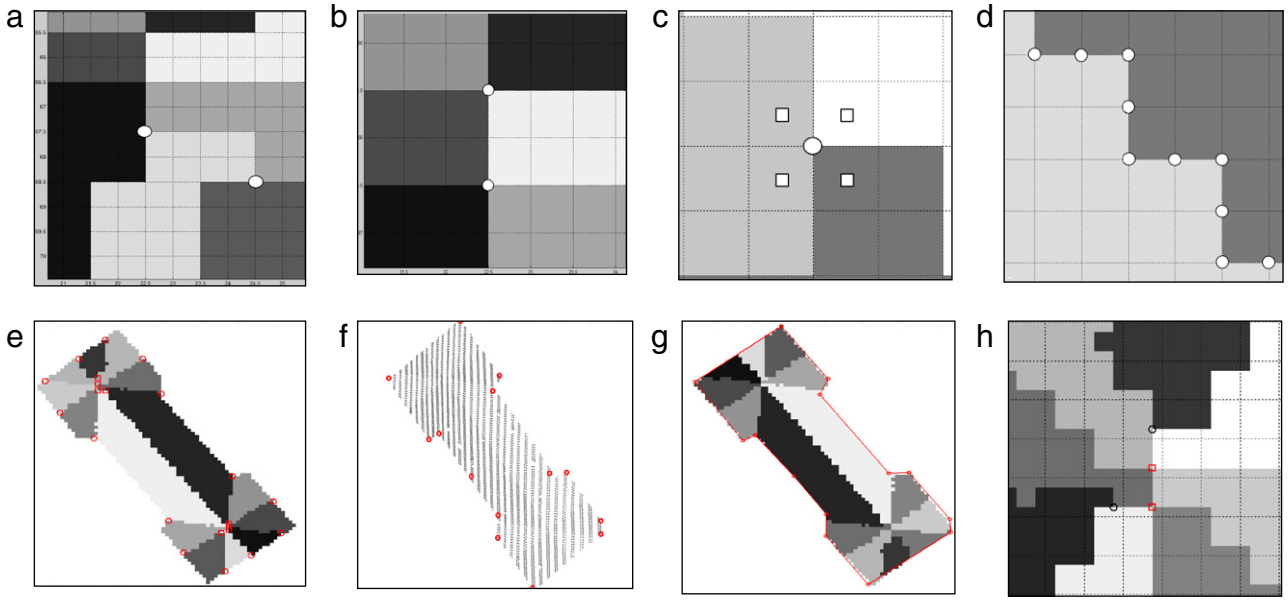

Fig. 6. Identification of roof structure points: (a) Case 1: points induced by three non-parallel planes; (b) Case 2: point induced by four roof planes; (c) Case 3: point induced by two roof planes (light and dark gray) and roof boundary; (d) Point on the roof ridge (not a roof structure point); (e) Identified roof structure points and their types (square: case 1 & 2; circle: case 3); (f) Reflection points; (g) Roof structure points induced by building boundary; (h) Four closely-located points.

0.5 pixels and check how many unique roof segments exist at four neighboring cells within ±0.25 intervals. In Fig. 6(a)–(d), four different cases are presented. White dots and squares denote grid points and their four neighboring cells, respectively.

If a grid point has at least three unique non-parallel roof segments in its neighborhood as shown in Fig. 6(a) and (b), it is considered as an intersection of corresponding roof segments. If two or three unique non-parallel roof segments and at least one building outside (dark blue) meet at a grid point (Fig. 6(c)), it is considered as an intersection of the corresponding roof segments and a vertical plane, which is determined from the building boundary. If only two unique non-parallel roof segments are found at a grid point as shown in Fig. 6(d), this point must lie on the roof ridge where two neighboring roof segments meet, and thus will not be considered as a roof structure point. The identified roof structure points are shown in Fig. 6(e) with different symbols. Although the 2D positions of these roof structure points may be different from their actual positions, they clearly imply which roof planes are adjacent and constitute roof structure points.

Based on this process, most of the roof structure points induced by the intersection of non-parallel roof segments are identified. To represent roof shape correctly, the intersection of two line segments of building boundary is also considered as a candidate for roof structure point. To determine these points, we first apply the α shape algorithm to trace the building boundary, followed by Douglas–Peucker algorithm. (Douglas and Peucker, 1973) to find reflection points as shown in Fig. 6(f). All boundary points between two consecutive reflection points are fitted to a line by RANSAC. Fig. 6(g) shows the candidate roof structure points determined by intersecting line segments on the building boundary. When some candidate roof structure points from these two groups are very close to each other as shown in Fig. 6(e) and (f), the points induced by non-parallel planes are used.

4.2. Positioning of roof structure points

In 3D space, three planes whose normal vectors are not coplanar intersect at exactly one point. By examining the number of unique roof segments and their normal vectors at each candidate roof structure point, its actual position in 3D space is determined through the following process. First, if a candidate roof structure point is adjacent to three non-parallel roof segments, e.g., Fig. 6(a), its actual 3D position is determined by intersecting these roof segments. If four unique roof segments are identified as in Fig. 6(b), the least squares approach is applied. For a candidate roof structure point induced by roof segments and boundary line segment as shown in Fig. 6(c), we define a vertical plane from the line segment, which has the shortest distance to the given intersection point. Then, the actual position is determined by plane intersection. When a cluster of estimated roof structure points are adjacent within a certain threshold (Fig. 6(h)), their arithmetic mean is taken as the final position of the structure point. For a candidate roof structure point induced from the line segments of building boundary, its height is assigned from the closest LiDAR point. Fig. 7(a) plots the determined roof structure points (in black) and raw LiDAR points.

For the 3D representation of a roof model, the remaining step is to determine the order of vertices, i.e., roof structure points, of each roof polygon. To achieve this, we again make use of a labeled image in 2D. We consider each roof segment $\bar{\Omega}_i$ as a binary image consisting of 1 and 0 for inside and outside roof plane, respectively. From the top left pixel of a roof segment, we sequentially follow the edge pixels. The order of the structure points is then defined by the sequential numbers of their corresponding closest pixels. This approach allows for determining vertices of any type of polygons in the correct order regardless of convex or non-convex shape. Fig. 7(b) illustrates this process. The same process is applied to all the roof segments. Finally, a 3D roof model is represented by assembling each roof segment polygon with its vertices and facades are generated by extruding line segments of the building boundary as shown in Fig. 7(c) For the final data structure, DCEL (Doubly Connected Edge List) is used. In this representation, vertices, edges, faces and all necessary connectivity information are maintained using three collections of records, i.e., vertices, half-edges and faces respectively. In the vertex record, each roof structure point is stored with its coordinates and a pointer to a half-edge which has this vertex as its origin. In the half-edge record, three roof ridges ($\mathrm{Twin}(\vec{e})$, $\mathrm{Next}(\vec{e})$, $\mathrm{Prev}(\vec{e})$), its vertex origin ($\mathrm{Origin}(\vec{e})$), and a face ($\mathrm{Face}(\vec{e})$) are stored. In the face record, a half-edge ($\vec{e}(f)$) of its exterior boundary is stored (Fig. 7(d)).

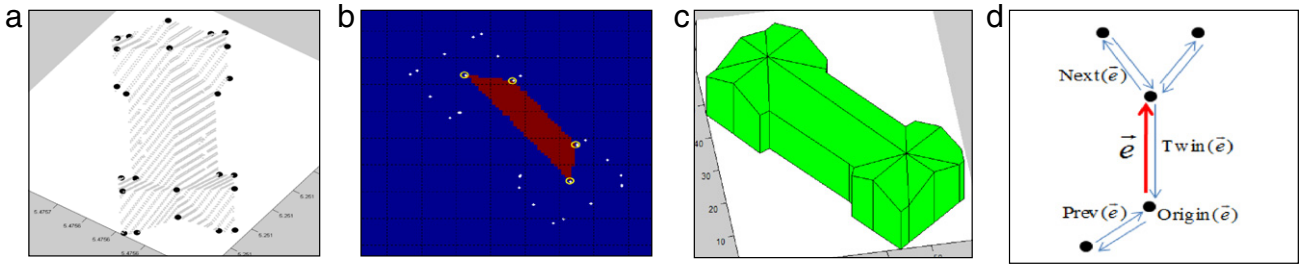

Fig. 7. Reconstruction of a 3D roof model: (a) Roof structure points; (b) Points on one roof plane; (c) Reconstructed roof model; (d) DCEL representation.

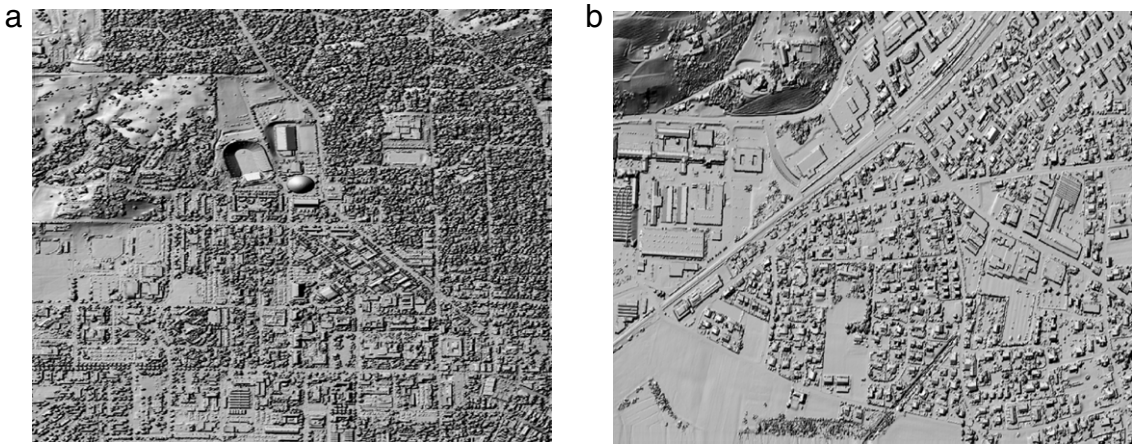

Fig. 8. Snapshots of the two tested data sets: (a) Purdue campus; (b) Heerbrugg, Switzerland.

Table 1
Summary of the two test data sets.

Location	Equipment	Date of acquisition	Average point density	# Returns	# Returns used
Purdue campus	Optech ALTM 1210	Spring 2001	≈1 pt/m^2	2	2
Heerbrugg, Switzerland	Leica ALS60	03/08/2009	≈4 pts/m^2	4	4

5. Tests and discussion

The proposed approach is applied to the two data sets summarized in Table 1 and shown in Fig. 8. A number of buildings are chosen from the LiDAR point clouds in each data set for evaluation. Fig. 9 presents the segmentation results and reconstructed roof models. The aerial photos (from GoogleMap) and shaded relief images (from the LiDAR points) are also presented to show overall roof structures. For all segmentation processes two level set functions are used in a recursive manner.

5.1. Evaluation of reconstructed buildings

Through a visual comparison of the segmented roof planes with the original LiDAR data, Table 2 shows the completeness of the nine (9) buildings in Fig. 9.

As shown in Table 2, some roof planes are missed in two extracted buildings (#1 and #2) in the Purdue data set. This is largely due to the coarse point density of this LiDAR data set. Most of the LiDAR points on the missed roof planes were identified as non-planar points (shown in Fig. 10) and excluded in the segmentation process.

The accuracy of a reconstructed roof model is described by the distances of LiDAR points to the segmented roof plane and the angular differences between their local normals and the plane segment normal. The distance and angular means are summarized in Table 3 for the roof planes of two buildings (#2 and #9). They measure how an extracted plane segment fits to the LiDAR points. These two discrepancies are apparently affected by LiDAR point density. The higher the density (Heerbrugg data set), the smaller size the neighboring LiDAR points occupy, which means more planarity of the neighborhood and thus the smaller distance disclosures. On the other hand, a smaller neighborhood size would cause larger uncertainty on the plane orientation, leading to larger angular differences as shown in Table 3. These two measures actually indicate the best separability that our approach can achieve.

We applied the proposed approach to a larger area in the Heerbrugg data set. The shaded relief of this area is presented in Fig. 11(a) along with building labels, while the reconstructed building models are shown in Fig. 11(b). It is seen that different roof types such as gable, hip, flat and a few more complex roofs are mixed in this area. All 20 buildings are reconstructed without difficulty except building #19, which has a dormer on its left side. Its 2D structure is represented in Fig. 12(a) The two points with solid circles are identified as roof structure points with three adjacent planes (P1, P2 and P3), while the other two points with open circles are not determined. For this reason, roof planes P2 and P3 cannot be reconstructed. In contrast, all roof structure points of a dormer connected with building boundary are identified correctly as in building #5 in Fig. 9. The problem of Fig. 12(a) is resolved as follows. Once all roof structure points (cases 1–3 shown in Fig. 6) are determined, the number of roof structure points of each roof plane are analyzed. Any roof plane with less than 3 roof structure points is identified. These are roof segments either standing alone or contained by another roof segment, which can therefore be traced as building boundary as discussed in

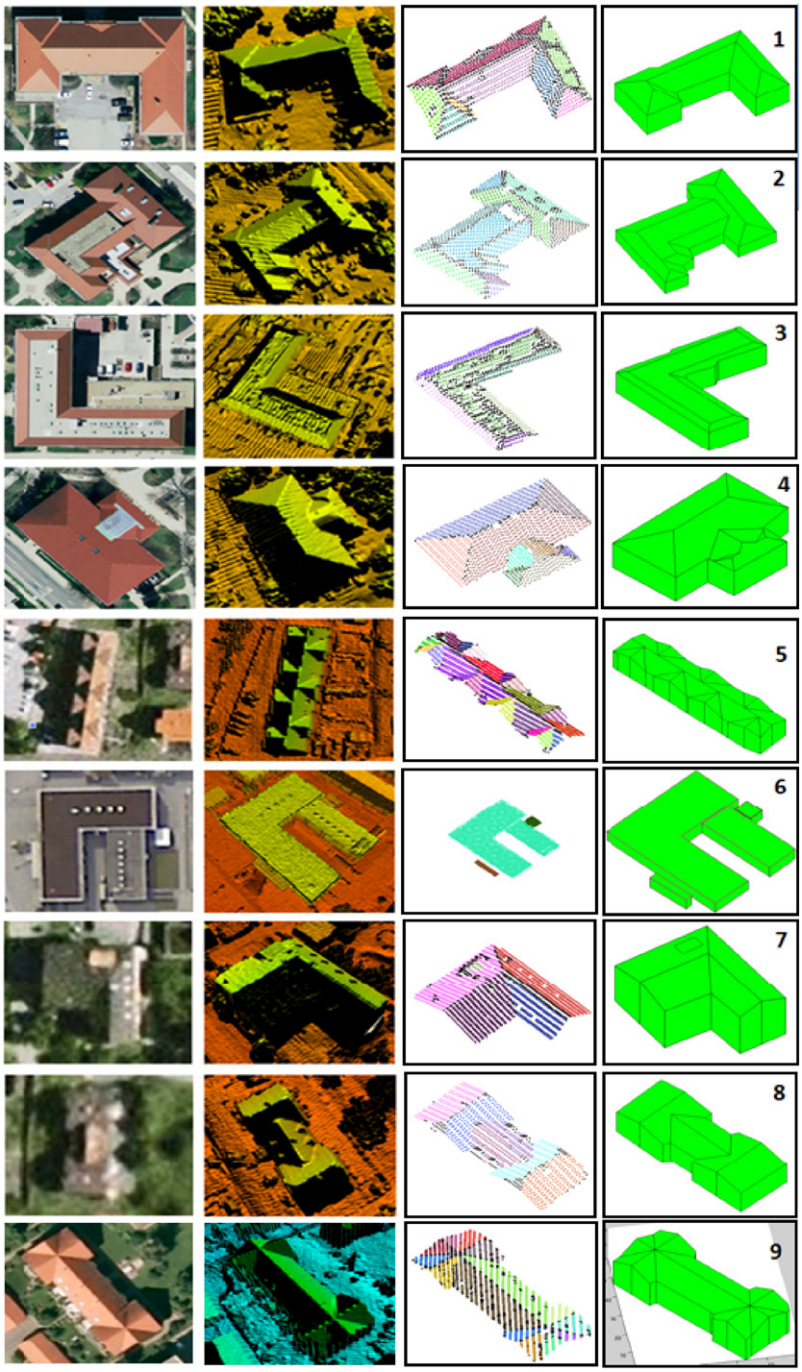

Fig. 9. Segmented roof and reconstructed roof models. From left to right: aerial photo, shaded relief, segmented roof (non-planar points with black dots), and roof model. (1)–(4): Purdue; (5)–(9): Heerbrugg.

Table 2
Completeness of reconstructed buildings.

Building #	# Segmented roof planes	# Roof planes in data	Completeness (%)
1	10	14	71.4
2	11	12	91.6
3	7	7	100
4	12	12	100
5	23	23	100
6	3	3	100
7	5	5	100
8	10	10	100
9	14	14	100
Mean			95.8

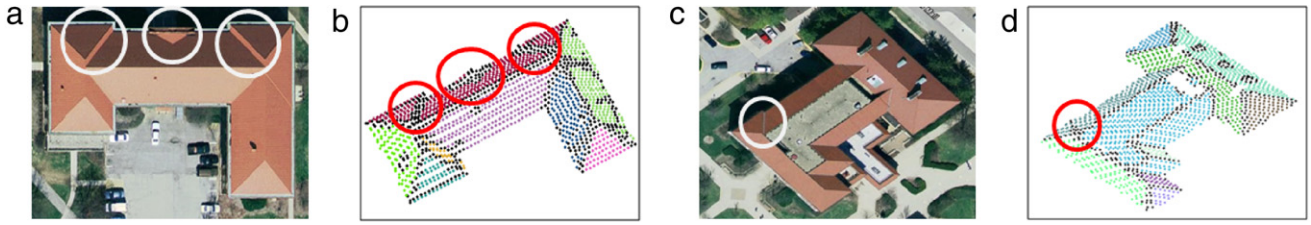

Fig. 10. Missed roof planes: (a) and (c) Locations of missed roof planes; (b) and (d) Non-planar points on the missed roof planes.

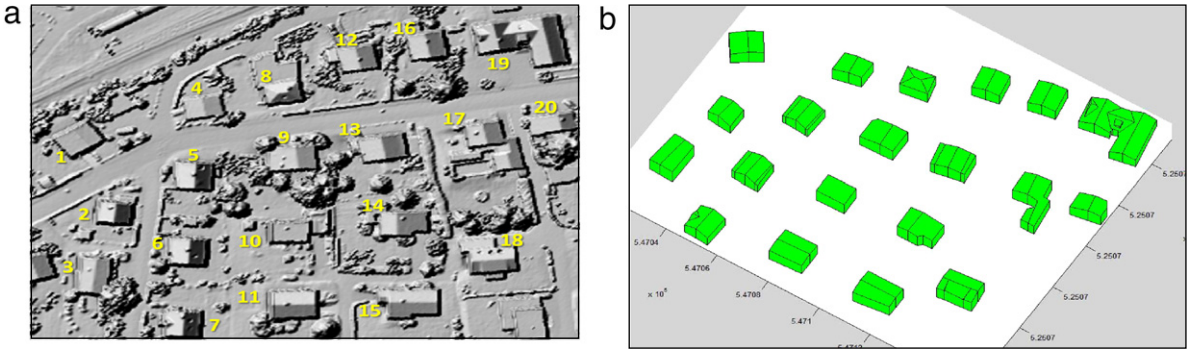

Fig. 11. A subset in Heerbrugg: (a) Shaded relief with identified building labels; (b) Reconstructed roof models.

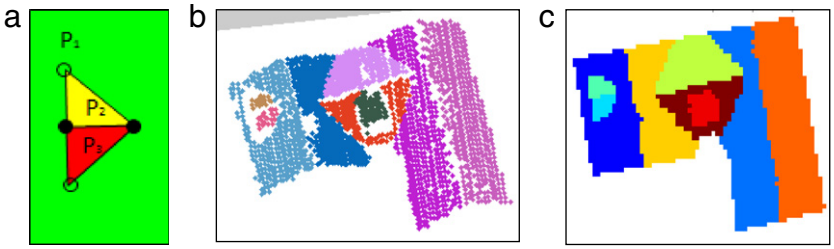

Fig. 12. Reconstruction of a dormer structure of building # 19: (a) Difficult case, (b) segmented points, (c) color coded planes.

Table 3
Accuracy of reconstructed building #2 and #9.

Roof #	Building #2 (Purdue)		Building #9 (Heerbrugg)	
	Distance (m)	Angular difference (°)	Distance (m)	Angular difference (°)
1	0.0267	3.87	0.0175	5.14
2	0.0316	5.11	0.0189	7.13
3	0.0275	2.75	0.0179	4.24
4	0.0256	2.85	0.0190	6.11
5	0.0186	2.14	0.0471	7.93
6	0.0888	4.42	0.0251	7.82
7	0.0293	3.11	0.0211	6.84
8	0.0263	2.46	0.0189	5.89
9	0.0282	3.68	0.0233	6.62
10	0.0343	2.82	0.0187	4.89
11	0.0199	1.88	0.0173	6.18
12	0.0263	2.74	0.0332	8.39
13	–	–	0.0181	5.63
14	–	–	0.0162	2.49
Mean	0.031	3.16	0.022	6.09

Section 4.1. Fig. 12(b) and (c) shows the segmented building points and color coded planes for building #19.

5.2. Computational performance

This section studies the effect of the number of data points, the number of grid cells, and initial level set functions on the computational performance of the proposed method, especially its convergence and computation time. The computation was carried out on a Core™2 Duo CPU 2.5 GHz using MATLAB program. Fig. 13(a)–(d) show regularly spaced initial zero level curves with four different radii, i.e., 9×, 5×, 3× and 2× the LiDAR point spacing, respectively. Fig. 13(e) shows the energy variation (convergence) in terms of the number of iterations. The labeled numbers in Fig. 13(e) are the same multiplication factors as in Fig. 13(a)–(d) (Figure for 7× is omitted). For each initial zero level curve, this program iterates for 50 times with a total execution time less than 20 s.

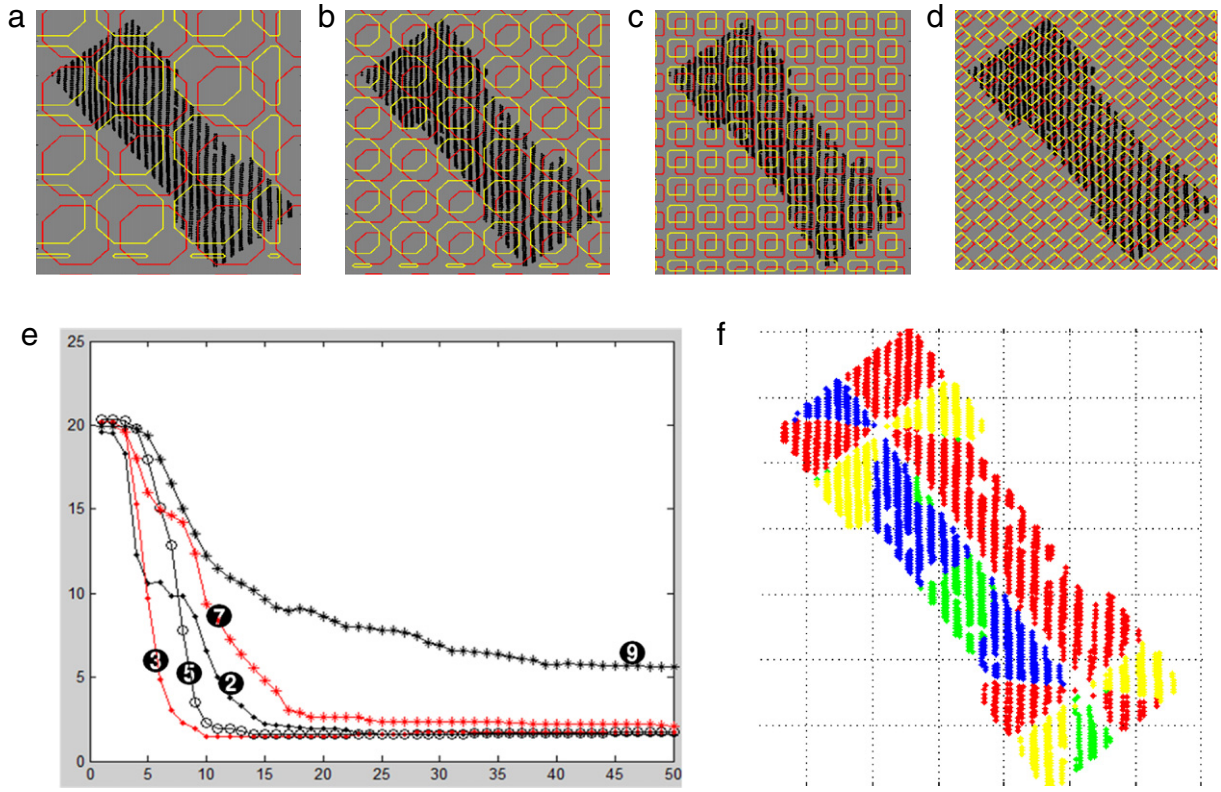

Fig. 13. Computational performance: (a)–(d) Initial zero level curves with different radii; (e) Convergence (energy function) versus the number of iterations under different initial radii; (f) Failure of convergence 9×.

Table 4
Computational performance of individual buildings.

Building #	n_p	$n_g = M \times N$	s/iteration	Total time (s)	Cells/s	Points/s
1	1029	47 × 69	0.18	1.08	17625	5716
2	1473	78 × 72	0.29	2.32	19365	5079
3	958	60 × 61	0.18	4.50	20333	5322
4	1333	58 × 44	0.21	2.31	12094	6347
5	1490	90 × 36	0.27	2.43	12000	5518
6	10466	129 × 127	1.70	32.30	9641	6156
7	2674	60 × 49	0.39	3.90	7596	6856
8	867	53 × 25	0.13	2.99	10351	6669
9	2631	78 × 69	0.44	4.40	12204	5979

Fig. 13(e) shows that the iteration converges generally faster with smaller radii for initial zero level curves. However, when the radii of initial zero level curves are too close to the LiDAR ground spacing, it may need more iteration, e.g., the case of 2× LiDAR ground spacing. On the other hand, larger radii, e.g., 9×, may even not produce correct segmentation result as shown in Fig. 13(f) (for comparison see Fig. 4(h)), since the minimization is trapped at the local minimum as shown in Fig. 13(e). By providing a larger number of initial zero level curves with the proper radius over the entire domain Ω, the segmentation process, e.g., breaking or merging of different regions is accelerated, which leads to faster convergence. Therefore, radius with 3–5× LiDAR ground spacing for initial zero level curves is recommended.

We also provide computational time for buildings shown in Fig. 9. The number of data points and grid cells in Ω are the most significant factors affecting the convergence time. Let n_p be the number of points and $n_g = M \times N$ be the number of grid cells in Ω. There are three main tasks per iteration: (1) identify all points $p_i \in P$ for a region and calculate its mean normal vector, (2) compute fitting terms, i.e. $H_\varepsilon(\phi_2^n)$ and $(1 - H_\varepsilon(\phi_2^n))$ in Eqs. (16) and (3) update level set functions. The 1st task has linear time complexity $O(n_p)$. The time for the 2nd task is $O(n_p \log n_p)$, while the 3rd task is simply updating a new ϕ^{n+1} with $O(n_g)$ complexity. Therefore, n_p is the main factor affecting the computation time. Table 4 gives the details about the nine buildings in Fig. 9 and their execution time.

Table 4 shows that the computation time is mostly proportional to n_p, about 5960 points per second per iteration. The computation time is affected by both the number of grid cells and the number of points, with the latter being more dominant. For example, though buildings #1 and #5 have almost the same number of grid cells, the larger number of points in building #5 leads to significantly slower calculation (0.27 vs. 0.18 s per iteration). In contrast, for buildings with similar number of data points, such as #7 and #9, a substantial increase (78×69 vs. 60×49) in the number of cells only causes minor extra computation cost (0.44 vs. 0.39 s per iteration). To reduce the number of grid cells, one may find the dominant building orientation and reorient it parallel to the coordinate axis.

5.3. Initial level set functions

Compared to the edge-based level set approach, the energy minimization problem introduced in this paper is more flexible for placing initial zero level curves (Chan and Vese, 2001). However, this minimization problem may not be convex, thus possibly leads

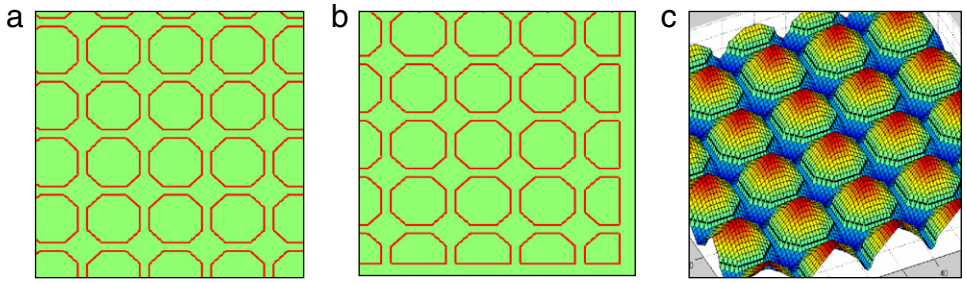

Fig. 14. Layout of initial level set functions: (a), (b) Regularly spaced zero level curves; (c) Initial level set function ϕ_1^0 represented as a signed distance function in 3D.

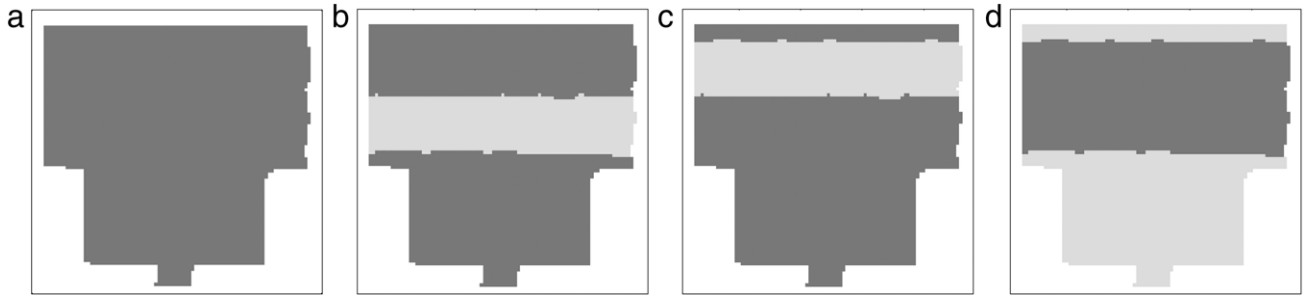

Fig. 15. Segmentation results from two level set functions: (a) R11 (empty); (b) R10; (c) R01; (d) R00.

to convergence at a local minimum. Defining the initial level set function from a set of regularly spaced zero level curves over the entire domain Ω is known to be helpful for finding the global minimum and reducing the processing time for convergence (Chan et al., 2000; Chan and Vese, 2001; Vese and Chan, 2002). Therefore, we define the initial level set function in the following way. First, a set of zero level curves with a fixed radius are placed regularly in Ω. In case of multiphase level set, these curves are placed with slight displacement to each other as shown in Fig. 13(a) and (b). Then, the value of a pixel is its distance to the closest zero level curve, with (+) for curve inside and (−) for curve outside, i.e.,

$$\phi_1^0(x,y) = \begin{Bmatrix} d((x,y),S) \text{ if } (x,y) \in S \\ -d((x,y),S) \text{ if } (x,y) \in S^c \end{Bmatrix} \quad (19)$$

where $\phi_1^0(x,y)$ is an initial value at location $\phi_1(x,y)$, S and S^c denote inside and outside of the zero level curves, and $d((x,y),S)$ is the distance between the point (x,y) and closest S. An example of initial level set function determined in this way is shown in Fig. 14(c) with 3D representation.

5.4. Number of level set functions

In the previous example shown in Fig. 4, the number of directional planes is the same as what two level set functions can produce, i.e., four directional planes are segmented with two level set functions. In this section, we will show that it is actually flexible in selecting the number of level set functions. We consider two different cases in which the number of segments in the data is (1) less than or (2) more than what the given number of level set functions can produce. In Fig. 15, there are three groups of directional roof planes. The original point clouds are shown in Fig. 5(a). Two level set functions produce three regions R10, R01 and R00 with the 1st region R11 being empty as shown in Fig. 15.

When more planar roof planes exist than what the given number of level set functions can segment, we apply the same segmentation process in a recursive manner. To demonstrate, only one level set function is applied to the same data shown in Fig. 15. This produces only two regions as shown in Fig. 16(a) and (b). It is seen that the 2nd region consists of one roof plane, whereas two groups of roof plans with different normal vectors are segmented into the 1st region, which needs to be further segmented. Once regions "1" and "2" are separated, we analyze the mean disclosure and mean angle difference of each $\bar{\Omega}_i$ for further possible segmentation. In this example, region "1" of Fig. 16(a) is further segmented with normal vectors first into two regions shown in Fig. 16(c) and (d). Region "3" shown in Fig. 16(c) is then further segmented with disclosures as feature vectors into two groups of parallel planes as shown in Fig. 16(e) and (f). Finally, region "4" in Fig. 16(e) is further separated into four roof primitives. The final segmentation result (total eight roof segments) and its reconstructed 3D model are presented in Fig. 16(g) and (h), respectively.

6. Conclusion

This paper treats roof modeling from airborne laser scanning data as a two-step task: segmentation and reconstruction. Segmentation is meant to find the roof geometric primitives, i.e., planar roof segments in this study, while reconstruction is to further determine their adjacency and integrity. Segmentation is approached by the method of multiphase and multichannel level set, which can simultaneously determine multiple segments. Two level set functions are used to segment up to four directional planes at a time and can be applied recursively for more complex roofs. Coplanar or parallel planes are further separated into individual roof segments through analyzing their connectivity and homogeneity. Finally, roof structure points are determined by intersecting adjacent roof segments and connected based on their topological relations inferred from the segmentation outcome.

The proposed approach has some distinctive properties. Compared to common region growing methods that only consider local planarity around a data point, this approach is global. This global nature also differentiates the proposed method from a RANSAC based approach which estimates parameters for one roof plane at a time. It simultaneously looks for multiple roof segments depending on the number of level set functions involved. For simple roof forms, e.g., gable, cross-gable, pyramid or hip roofs, correct segmentation can be achieved within a few iterations with two level set functions. As many other clustering methods,

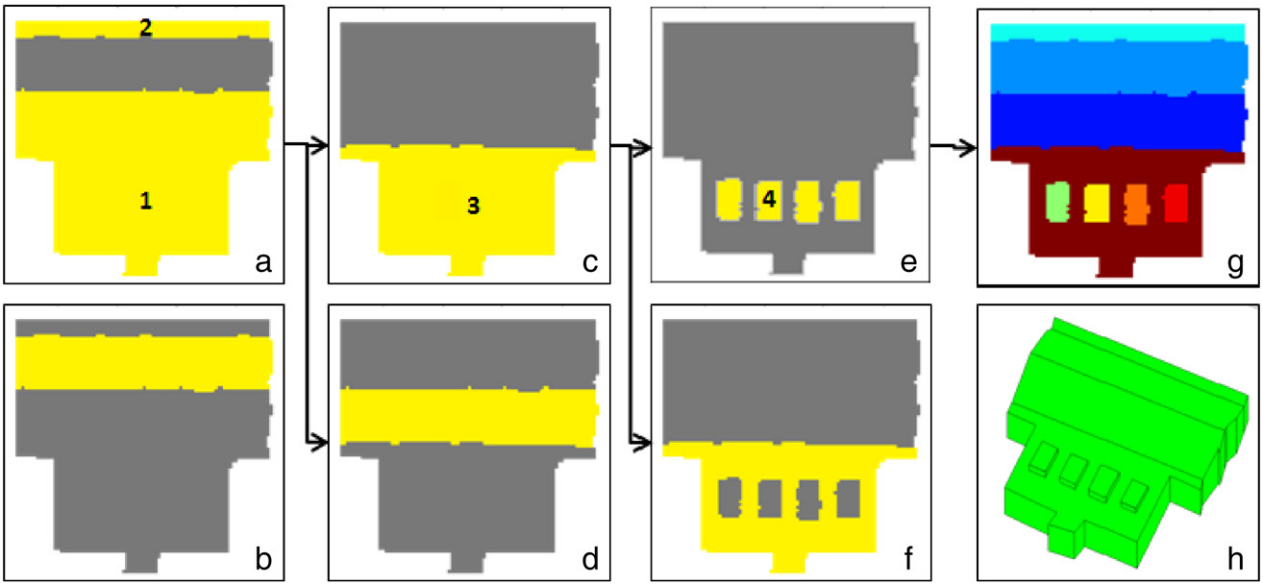

Fig. 16. Recursive segmentation with one level set function: (a) and (b) Initial segmentation results; (c) and (d) Recursive segmentation of region "1"; (e) and (f) Recursive segmentation of region "3"; (g) Segmentation result; (h) Reconstructed model.

the framework of multiple level set can be used recursively to segment more complex building roofs. All recursive segmentations in our experiments proceeded to resolving under-segmentation problem. On the contrary, over-segmentation problem, which is more problematic case in this study, occurred when the segmentation is trapped at the local minimum. This issue is largely minimized by defining multiple initial zero level curves presented in this paper. It is also found that 3–5× LiDAR ground spacing among these curves is appropriate, with larger spacing leading to possible incorrect convergence and smaller spacing to slower computation. In the context of segmentation accuracy and detail, our experiments show promising results. However, like most other approaches, the results are affected by parameters involved. For example, the mean angle difference used for determining the homogeneity of segments clearly restricts further segmentation. Another property is that it always produces connected segments and their boundaries correspond to roof ridges or step edges, which facilitates the determination of topologic relations among the roof segments and thus benefits 3D roof reconstruction. This is different from *k*-means clustering based methods, which only deal with LiDAR points in feature space.

The proposed approach also has some limitations at the present stage. Similar to other approaches, point clouds involved in the method are largely building points. This requires the separation of building points from others as exact as possible. This is an active research topic and not dealt with in detail in this work. As a common limitation of data-driven approach for building reconstruction, the completeness of 3D reconstruction depends on the average point density of the input point clouds. If there are not enough data points to represent roof structures, they will not be segmented correctly. In this study, most roof planes are segmented without recursive process and only a few are fully segmented at the third recursive step. Therefore, more tests with different roof forms and complex buildings should be continued.

Acknowledgements

The authors would like to thank the reviewers whose constructive comments and suggestions improved the clarity of the paper. Also, it is grateful to acknowledge that Dr. George Vosselman voluntarily provided his segmentation results that helped us in finalizing our implementation and presentation.

References

Alharthy, A., Bethel, J., 2002. Heuristic filtering and 3D feature extraction from LiDAR data. International Archives of Photogrammetry, Remote Sensing and Spatial Information Sciences 34 (Part 3/A), 29–34.
Arefi, H., Hahn, M., 2005. A morphological reconstruction algorithm for separating off-terrain points from terrain points in laser scanning data. International Archives of Photogrammetry, Remote Sensing and Spatial Information Sciences 36 (Part 3/W19), 120–125.
Aubert, G., Vese, L., 1997. A variational method in image recovery. SIAM Journal on Numerical Analysis 34 (5), 1948–1979.
Ayed, I.B., Mitiche, A., Belhadj, Z., 2005. Multiregion level-set partitioning of synthetic aperture radar images. IEEE Transactions on Pattern Analysis and Machine Intelligence 27 (5), 793–800.
Behan, A., 2000. On the matching accuracy of rasterised scanning laser altimeter data. International Archives of Photogrammetry and Remote Sensing 33 (Part 2B), 75–80.
Cao, G., Yang, X., 2007. Man-made object detection in aerial images using multi-stage level set evolution. International Journal of Remote Sensing 28 (8), 1747–1757.
Cao, G., Yang, X., Mao, Z., 2005. A two-stage level set evolution scheme for man-made objects detection in aerial images. In: Proceedings of the IEEE Computer Society Conference on Computer Vision and Pattern Recognition, pp. 474–479.
Chan, T.F., Sandberg, B.Y., Vese, L.A., 2000. Active contours without edges for vector-valued images. Journal of Visual Communication and Image Representation 11 (2), 130–141.
Chan, T.F., Vese, L.A., 2001. Active contours without edges. IEEE Transactions on Image Processing 10 (2), 266–277.
Douglas, D., Peucker, T., 1973. Algorithms for the reduction of the number of points required to represent a digitized line or its caricature. Cartographica: The International Journal for Geographic Information and Geovisualization 10 (2), 112–122.
Edelsbrunner, H., Kirkpatrick, D., Seidel, R., 1983. On the shape of a set of points in the plane. IEEE Transactions on Information Theory 29 (4), 551–559.
Forlani, G., Nardinocchi, C., Scaioni, M., Zingaretti, P., 2006. Complete classification of raw LiDAR data and 3D reconstruction of buildings. Pattern Analysis & Applications 8 (4), 357–374.
Haralick, R.M., Shapiro, L.G., 1992. Computer and Robot Vision, vol. 1. Addison-Wesley, Boston, MA, pp. 672.
Horritt, M.S., 1999. A statistical active contour model for SAR image segmentation. Image and Vision Computing 17 (3–4), 213–224.
Karantzalos, K., Paragios, N., 2008. Automatic model-based building detection from single panchromatic high resolution images. International Archives of Photogrammetry, Remote Sensing and Spatial Information Sciences 37 (Part B3a), 127–132.
Maas, H., Vosselman, G., 1999. Two algorithms for extracting building models from raw laser altimetry data. ISPRS Journal of Photogrammetry and Remote Sensing 54 (2–3), 153–163.
Osher, S., Sethian, J.A., 1988. Fronts propagating with curvature dependent speed: algorithms based on Hamilton–Jacobi formulations. Journal of Computational Physics 79 (1), 12–49.
Oude Elberink, S., Maas, H.G., 2000. The use of anisotropic height texture measures for the segmentation of airborne laser scanner data. International Archives of Photogrammetry, Remote Sensing and Spatial Information Sciences 33 (Part B3), 678–684.

Oude Elberink, S., Vosselman, G., 2009. Building reconstruction by target based graph matching on incomplete laser data: analysis and limitations. Sensors 9 (8), 6101–6118.

Rottensteiner, F., 2003. Automatic generation of high-quality building models from LiDAR data. IEEE Computer Graphics and Applications 23 (6), 42–50.

Rottensteiner, F., Briese, C., 2002. A new method for building extraction in urban areas from high-resolution LiDAR data. International Archives of Photogrammetry, Remote Sensing and Spatial Information Sciences 34 (Part 3/A), 295–301.

Rudin, L., Osher, S., Fatemi, E., 1992. Nonlinear total variation based noise removal algorithms. Physica D 60 (1–4), 259–268.

Sampath, A., Shan, J., 2007. Building boundary tracing and regularization from airborne LiDAR point clouds. Photogrammetric Engineering and Remote Sensing 73 (7), 805–812.

Sampath, A., Shan, J., 2010. Segmentation and reconstruction of polyhedral building roofs from aerial LiDAR point clouds. IEEE Transactions on Geoscience and Remote Sensing 48 (3), 1554–1567.

Sethian, J.A., 1990. Numerical algorithms for propagating interfaces: Hamilton–Jacobi equations and conservation laws. Journal of Differential Geometry 31 (38), 131–161.

Shan, J., Sampath, A., 2005. Urban DEM generation from raw LiDAR data: A labeling algorithm and its performancee. Photogrammetric Engineering and Remote Sensing 71 (2), 217–226.

Sithole, G., Vosselman, G., 2004. Experimental comparison of filter algorithms for bare-Earth extraction from airborne laser scanning point clouds. ISPRS Journal of Photogrammetry and Remote Sensing 59 (1–2), 85–101.

Song, Y., Shan, J., 2008. Building extraction from high resolution color imagery based on edge flow driven active contour and JSEG. International Archives of Photogrammetry, Remote Sensing and Spatial Information Sciences 37 (Part B3a), 185–190.

Tarsha-Kurdi, F., Landes, T., Grussenmeyer, P., 2007. Hough-transform and extended RANSAC algorithms for automatic detection of 3D building roof planes from LiDAR data. In: Proceedings of the ISPRS Workshop on Laser Scanning 2007 and SilviLaser 2007, Espoo, Finland, pp. 407–412.

Tarsha-Kurdi, F., Landes, T., Grussenmeyer, P., 2008. Extended RANSAC algorithm for automatic detection of building roof planes from LiDAR data. Photogrammetric Journal of Finland 21 (1), 97–109.

Verma, V., Kumar, R., Hsu, S., 2006. 3D Building detection and modeling from aerial LiDAR data. In: Proceedings of the 2006 IEEE Computer Society Conference on Computer Vision and Pattern Recognition. CVPR'06. IEEE Computer Society, Washington, DC, pp. 2213–2220.

Vese, L.A., Chan, T.F., 2002. A multiphase level set framework for image segmentation using the Mumford and Shah model. International Journal of Computer Vision 50 (3), 271–293.

Vosselman, G., Dijkman, S., 2001. 3D building model reconstruction from point clouds and ground plans. International Archives of Photogrammetry, Remote Sensing and Spatial Information Sciences 34 (Part 3/W4), 37–43.

Vosselman, G., Gorte, B.G.H., Sithole, G., Rabbani, T., 2004. Recognising structure in laser scanner point clouds. International Archives of Photogrammetry. Remote Sensing and Spatial Information Sciences 46 (Part 8/W2), 33–38.

Wang, J., Shan, J., 2009. Segmentation of LiDAR point clouds for building extraction. In: Proceedings of the ASPRS 2009 Annual Conference, Baltimore, MD, USA (on CD-ROM).

Wei, S., 2008. Building boundary extraction based on LiDAR point clouds data. International Archives of Photogrammetry, Remote Sensing and Spatial Information Sciences 37 (Part B3b), 157–162.

Zhang, J.R., Jiang, X.Z., 2008. Research on Edge Extraction with Level Set Method. International Archives of Photogrammetry, Remote Sensing and Spatial Information Sciences 37 (Part B4), 433–438.

Zhang, K., Chen, S., Whitman, D., Shyu, M., Yan, J., Zhang, C., 2003. A progressive morphological filter for removing nonground measurements from airborne LIDAR data. IEEE Transactions on Geoscience and Remote Sensing 41 (4), 872–882.

Zhao, H.K., Chan, T., Merriman, B., Osher, S., 1996. A variational level set approach to multiphase motion. Journal of Computational Physics 127 (1), 179–195.

Zhou, Q.Y., Neumann, U., 2008. Fast and extensible building modeling from airborne LiDAR data. In: Proceedings of the 16th ACM SIGSPATIAL International Conference on Advances in Geographic Information Systems. ACM GIS 2008 (on CD-ROM).